



Article

Electro-Sorption of Hydrogen by Platinum, Palladium and Bimetallic Pt-Pd Nanoelectrode Arrays Synthesized by Pulsed Laser Ablation

Antonino Scandurra ^{1,2,3,*} , Maria Censabella ^{1,2}, Antonino Gulino ^{3,4} , Maria Grazia Grimaldi ^{1,2} and Francesco Ruffino ^{1,2,3}

- ¹ Department of Physics and Astronomy “Ettore Majorana”, University of Catania, Via Santa Sofia 64, 95123 Catania, Italy; maria.censabella@ct.infn.it (M.C.); mariagrazia.grimaldi@ct.infn.it (M.G.G.); francesco.ruffino@ct.infn.it (F.R.)
- ² Institute for Microelectronics and Microsystems of National Research Council of Italy (CNR-IMM), Via Santa Sofia 64, 95123 Catania, Italy
- ³ Research Unit of the University of Catania, National Interuniversity Consortium of Materials Science and Technology (INSTM-UdR of Catania), Viale Andrea Doria 8 and Via S. Sofia 64, 95125 Catania, Italy; agulino@unict.it
- ⁴ Department of Chemical Sciences, University of Catania, Viale Andrea Doria 6, 95123 Catania, Italy
- * Correspondence: ascandurra@unict.it

Abstract: Sustainable and renewable production of hydrogen by water electrolyzers is expected to be one of the most promising methods to satisfy the ever-growing demand for renewable energy production and storage. Hydrogen evolution reaction in alkaline electrolyte is still challenging due to its slow kinetic properties. This study proposes new nanoelectrode arrays for high Faradaic efficiency of the electro-sorption reaction of hydrogen in an alkaline electrolyte. A comparative study of the nanoelectrode arrays, consisting of platinum or palladium or bimetallic nanoparticles (NPs) Pt₈₀Pd₂₀ (wt.%), obtained by nanosecond pulsed laser ablation in aqueous environment, casted onto graphene paper, is proposed. The effects of thin films of perfluoro-sulfonic ionomer on the material morphology, nanoparticles dispersion, and electrochemical performance have been investigated. The NPs-GP systems have been characterized by field emission scanning electron microscopy, Rutherford backscattering spectroscopy, X-ray diffraction, X-ray photoelectron spectroscopy, cyclic voltammetry, and galvanostatic charge-discharge cycles. Faradaic efficiency up to 86.6% and hydrogen storage capacity up to 6 wt.% have been obtained by the Pt-ionomer and Pd/Pt₈₀Pd₂₀ systems, respectively.

Keywords: pulsed laser ablation; nanoparticles; platinum; palladium; bimetallic Pt-Pd; electrochemical hydrogen storage



Citation: Scandurra, A.; Censabella, M.; Gulino, A.; Grimaldi, M.G.; Ruffino, F. Electro-Sorption of Hydrogen by Platinum, Palladium and Bimetallic Pt-Pd Nanoelectrode Arrays Synthesized by Pulsed Laser Ablation. *Micromachines* **2022**, *13*, 963. <https://doi.org/10.3390/mi13060963>

Academic Editor:
Nam-Trung Nguyen

Received: 28 May 2022

Accepted: 16 June 2022

Published: 18 June 2022

Publisher's Note: MDPI stays neutral with regard to jurisdictional claims in published maps and institutional affiliations.



Copyright: © 2022 by the authors. Licensee MDPI, Basel, Switzerland. This article is an open access article distributed under the terms and conditions of the Creative Commons Attribution (CC BY) license (<https://creativecommons.org/licenses/by/4.0/>).

1. Introduction

One of the most important challenges in the development of green energy production and storage is represented by the critical mineral commodities [1]. The list of the strategic minerals for new and emerging technologies could change with time; the most valuable elements include, but are not limited to, lithium, arsenic, gallium, germanium, indium, tellurium, rare-earth elements and cobalt [2]. Those raw materials are strategic for the development of green energy production and storage, but have a high-risk associated with their supply [2]. Moreover, their extraction often produces serious environmental impact and high amount of clean water consumption [3].

Renewable hydrogen production through electro-catalytic water splitting is of paramount importance as sustainable and renewable energy technology can help to overcome the above risks [4]. However, there are currently significant problems in hydrogen-based technology which are represented by the actual technological limits for green production, storage and then distribution. [5–7]. Moreover, from an industrial point of view, water splitting in

alkaline electrolyte is more appealing, since it overcomes the problem of expensive proton exchange membranes required in acidic electrolytes. Unfortunately, the water splitting in alkaline electrolyte is still challenging due to its slow kinetic properties [8].

Several classes of hybrid nanomaterials have been reported in the literature both for the hydrogen production as well as for its storage at low pressure and ambient temperature [9–11]. Compared to the hydrides of metal alloys, the systems based on inorganic electro-catalytic nanomaterials supported onto a carbon matrix are more attractive due to, for instance, their lightweight [12]. Platinum and palladium, particularly in the form of nanoparticles (NPs), are highly efficient electro-catalysts for the hydrogen evolution reaction (HER) by water splitting. Furthermore, they are also hydrogen's absorbers [13–19].

Metal NPs prepared by conventional wet chemistry are typically obtained by reduction of a metal precursor by sodium borohydride, or ascorbic acid or ethylene glycol [20]. NPs obtained by chemical reduction may have the surface covered by ligands, surfactants or other unwanted by-products of the reduction reaction. Furthermore, the nanoparticles could be unintentionally doped, incorporating metal ions that limit their electro-catalytic activity. [20]. Conversely, pulsed laser ablation in liquid environment (PLAL) is a versatile and environmentally friendly technique that overcomes the limitation of purity and surface cleanliness present in the NPs produced by conventional wet processes. PLAL is suitable for metal NPs fabrication with a ligand-free surface [21–24]. In the PLAL method, a laser beam is focused by an optical system on a solid target in a liquid environment, typically water, then the radiation absorbed by the target leads to the formation of an expanding plasma plume, which contains the ablated material and results in a nanoparticle suspension [25]. Moreover, by changing the parameters of the laser (fluence, wavelength, pulse duration) or the liquid media it is possible to obtain nanoparticles with tailored size, physicochemical and morphological properties [25–27].

Furthermore, the improvement of the energy efficiency of the electrolysis process in alkaline electrolyte can be obtained by a proper designed ionomer membrane, acting as proton permeable materials or separator [28]. Recently, Hodges and co-workers proposed a porous inter-electrode separator of polyethersulfone 8 μm thick for a capillary-fed electrolysis cell, thus obtaining cost-competitive water splitting in alkaline electrolyte characterized by an energy efficiency of 98% [28].

In this paper we characterized three low-cost systems consisting of novel hybrid nano-electrode arrays of platinum or palladium or Pt-Pd nanoparticles, obtained by PLAL, supported onto graphene paper (GP) [29,30]. Moreover, the effects of a thin proton permeable membrane, enclosing the metal NPs, on the Faradaic efficiency of the electro-sorption reaction of hydrogen in alkaline electrolyte are discussed.

2. Materials and Methods

2.1. Materials and NPs-GP Preparation

Potassium hydroxide 99.99%, sodium perfluoro-sulfonate ionomer (NafionTM) 5 wt.% solution, and graphene paper 240 μm thick were purchased from Sigma Aldrich Merck (Milan, Italy). NPs suspensions of platinum, palladium and Pt₈₀Pd₂₀ (wt.%) were prepared by PLAL in water treated in a MilliQTM system, characterized by a total organic carbon (TOC) of ≤ 5 part per billion (ppb) and resistivity of 18.2 M Ω cm. The composition of the Pt₈₀Pd₂₀ (wt.%) alloy was chosen on the basis of its stability during the laser ablation as sputter target. The detailed methodology, the experimental setup and the conditions used for the NPs preparation were reported in a previous work [30]. NPs-GP nanoelectrode arrays were obtained using pieces of GP of 1 cm \times 3 cm. Then, the water-based NPs suspensions were drop casted onto 1 cm² of both sides of GP in hot plate at 100 °C, in air. In details, 29 $\mu\text{g cm}^{-2}$ of platinum, or 5 $\mu\text{g cm}^{-2}$ of palladium, or 5 $\mu\text{g cm}^{-2}$ of Pt₈₀Pd₂₀ NPs were deposited, obtaining three different sample batches, respectively. The remaining part of the electrode was isolated from the solution by adhesive tape. Another set of nanoelectrode arrays were prepared by drop casting the NPs in water-0.25 wt.% of Nafion suspensions. The latter suspensions were prepared by adding later the stock

solution of 5 wt.% Nafion to the water-based NPs suspensions. The estimated average thickness of Nafion film, assuming a density of 1.8 g cm^{-3} for partially hydrated Nafion, is of $0.7 \text{ }\mu\text{m}$ [31].

2.2. Instrumental Characterization

NPs-GP morphology was investigated by field emission scanning electron microscopy (FE-SEM). A Gemini 152 Carl Zeiss Supra 25 instrument (Jena, Germany) was used. Typically, the analyses were carried out by an acceleration voltage of 5 kV and an aperture size of $30 \text{ }\mu\text{m}$, a working distance of 3 mm, and using an In-lens detector. Transmission Electron Microscopy (TEM) analyses were obtained by a 2010 JEOL Instrument (3-1-2 Musashino, Akishima, Tokyo 196-8558, Japan) employing 200 KeV accelerating voltage. NPs size distribution was determined by the images analysis, using the Gatan Digital Micrograph software version 3.9 (Pleasanton, CA 94588 United States). The mean value of the NPs diameter, $\langle D \rangle$, for each sample has been calculated on a statistical population of 900 particles. The associated error consists of the standard deviation on the mean value [30]. 3.5 MV HVEE (High Voltage Engineering Europa, Amersfoort, The Netherlands) Singletron accelerator system was used for the Rutherford Backscattering Spectrometry (RBS) measurements. X-ray diffraction (XRD) measurements were obtained using a Smartlab Rigaku diffractometer (Matsubara-cho, 3-9-12 Akishima-shi, Tokyo, Japan) operating in Bragg-Brentano mode. The X-ray source of Cu $K\alpha$ radiation with a rotating anode operated at 45 kV and 200 mA.

X-ray photoelectron spectra (XPS) were measured by a PHI 5000 Versa Probe II system ULVAC-PHI, Inc. (2500 Hagisono, Chigasaki, Kanagawa, 253-8522, Japan), and were excited by monochromatized Al $K\alpha$ X-ray radiation. The photoelectrons were collected at take-off angle of 45° relative to the surface sample holder. The base pressure of the main chamber was $1 \times 10^{-8} \text{ Pa}$ [32,33]. The instrumental energy resolution was $\leq 0.5 \text{ eV}$ at pass energy of 5.85 eV. The XPS peak intensities were obtained after Shirley background removal. Binding energy scale calibration was achieved by fixing the graphene C 1s main peak at 284.6 eV [32,33]. The atomic concentration analysis was obtained by the peak intensities considering the relevant atomic sensitivity factors [34]. Some X-ray photoelectron spectra were fitted with symmetrical Gaussian envelopes, after subtraction of the background. Data refinement of the fitting process was based on the method of the least squares fitting, carried out until there was the highest possible correlation between the experimental spectrum and the theoretical profile. The residual or agreement factor R, defined by $R = [\sum (\text{Fobs} - \text{Fcalc})^2 / \sum (\text{Fobs})^2]^{1/2}$, after minimization of the function $\sum (\text{Fobs} - \text{Fcalc})^2$, converged to the value of 0.03 [34].

Electrochemical measurements were performed by Versastat 4 Princeton Applied Research potentiostat (801 South Illinois Avenue Oak Ridge TN, 37830 United States) in air, at 25°C . Saturated Calomel Electrode (SCE) and platinum electrode were used as reference and counter, respectively. 30 mL of fresh, not de-aerated solution of KOH 1 M was used for each measurement. The electro-catalytic properties of nanostructures towards hydrogen evolution reaction and storage were studied by Cyclic Voltammetry (CV) at scan rate of 20 mVs^{-1} and galvanostatic charge-discharge curved at a current of $-100/+100 \text{ }\mu\text{A}$, respectively. The duration of a single charge-discharge cycle was of 600 s.

3. Results

3.1. Morphology of NPs-GP Nanoelectrode Arrays

Figure 1a–c report the TEM images of the Pt, Pd and $\text{Pt}_{80}\text{Pd}_{20}$ NPs, respectively. The shape of the NPs is almost spherical and the average size is $10 \pm 2 \text{ nm}$ for Pt, $12 \pm 2 \text{ nm}$ for palladium and $11 \pm 5 \text{ nm}$ for $\text{Pt}_{80}\text{Pd}_{20}$, respectively. More detailed analysis of the NPs has been reported in a previous work by the authors [30]. Figure 2a–c report the morphology, studied by FE-SEM, of the NPs-GP composite systems obtained by water-based suspensions of Pt, Pd and $\text{Pt}_{80}\text{Pd}_{20}$ NPs, respectively. It is worthy of note that the FE-SEM pictures of Figure 2a–c show the presence of some larger NPs than those shown in the TEM pictures.

The reason of this apparent discrepancy is due to the tail in the size distributions presented by the PLAL synthesized nanoparticles [27,30].

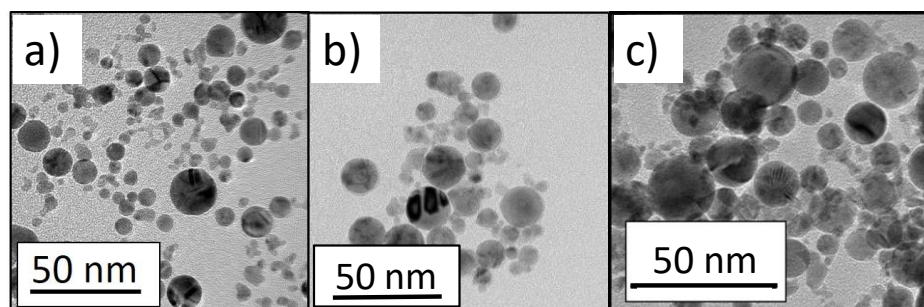


Figure 1. Transmission electron microscopy image of: (a) Pt, (b) Pd and (c) Pt₈₀Pd₂₀ nanoparticles.

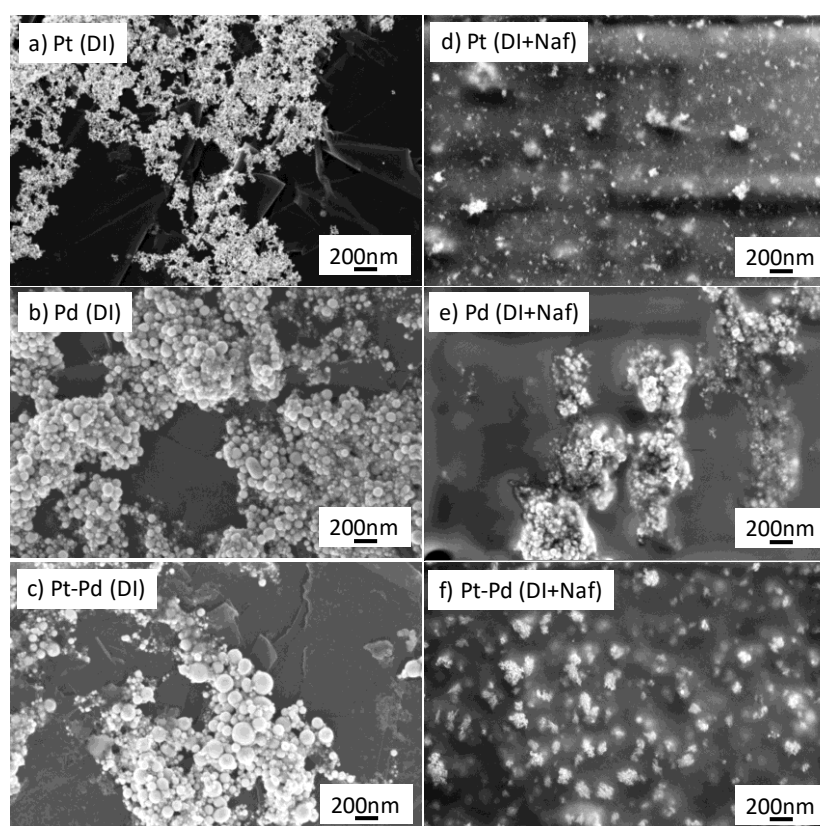


Figure 2. Field emission scanning electron microscopy pictures of NPs-GP nanocomposites: (a–d) Pt in deionized water and in Nafion solution; (b–e) Pd in deionized water and in Nafion solution; (c–f) Pt₈₀Pd₂₀ in deionized water and in Nafion solution.

Figure 2d–f show the FE-SEM morphology of the NPs-GP composite systems obtained by casting NPs suspension in water containing 0.25% wt. of Nafion. Clearly, the Nafion contribute significant to the dispersion of NPs on the surface. The dispersion is produced by the negatively charged sulphonic groups of Nafion which are present on the surface of the coated NPs and, therefore, repel them from each other and avoid their aggregation. This result is of relevant importance in the electrochemical behavior of the PN-GP towards hydrogen production and storage (vide later on).

Figure 3a–c shows the RBS spectra of the NPs-GP systems. RBS spectra were simulated by using XRump software, [35] which furnished the composition and identified the element present on the outermost layer of surface. The spectra show signals of C, O, S, Na, Pd, and Pt, as marked in the following Figure (simulation not shown). The spectra of the NPs-GP

systems obtained by water suspension show a weak signal of sodium, whose origin may be attributed to the process of GP fabrication. Furthermore, the metal nanoparticles produce sharp peaks of the backscattered He^+ ions thus confirming the homogeneity and contiguity of the NPs arrays. In contrast, the presence of Nafion produces a significant broadening of the peaks associated to the metal nanoparticles, with a tail on the lower side of the energy scale. The low energy tail in the spectra (below 1.6 MeV) is attributed to metal NPs enclosed in the Nafion film [36].

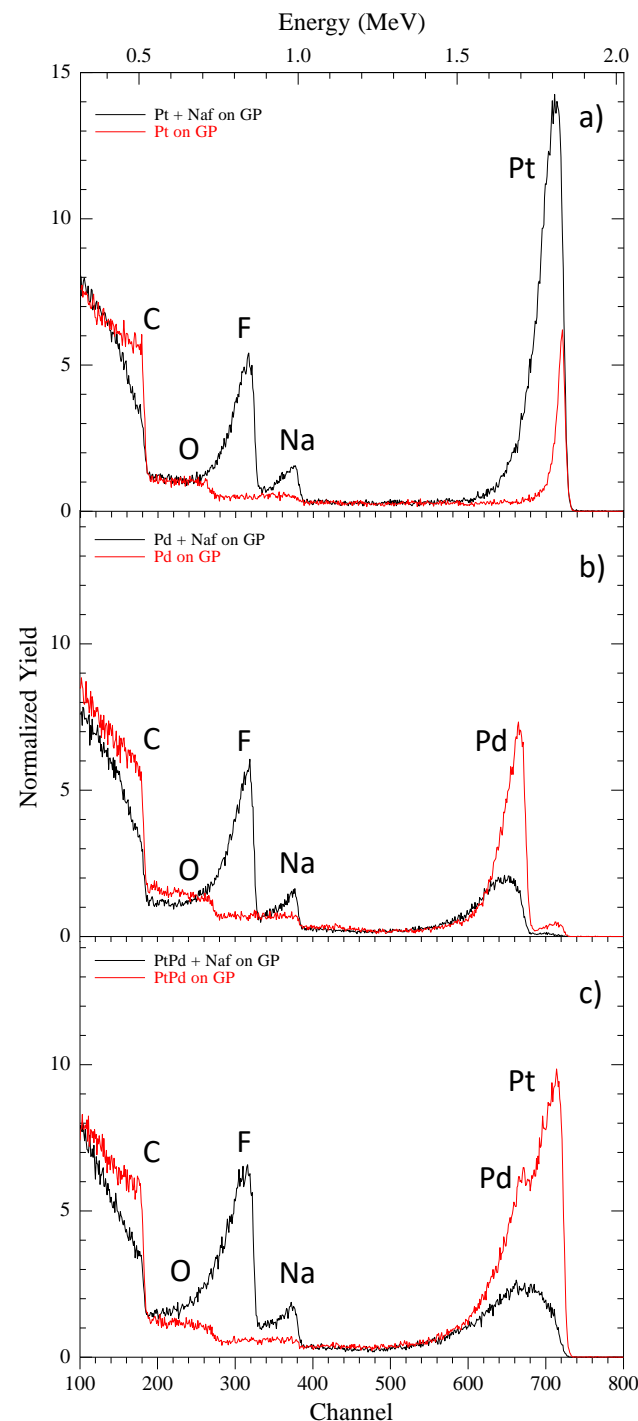


Figure 3. Rutherford backscattering spectra of NPs-GP composite systems obtained by water (red lines) and water-0.25% wt. Nafion suspensions (black lines): (a) Pt; (b) Pd; (c) $\text{Pt}_{80}\text{Pd}_{20}$.

3.2. Structure of PLAL NPs

Figure 4 shows the XRD patterns of the platinum, palladium and Pt₈₀Pd₂₀ NPs-GP composite systems. The XRD patterns show the signal at 2θ with the values of 44.52, 54.66, 59.85, 71.47, 77.40, 83.53, corresponding to 101, 004, 103, 104, 110, 112 reflections which are assigned to the graphitic phase of the GP [37]. The patterns in Figure 4 do not contain specific features to be attributed to single graphene layers or graphene oxides. Additional peaks (marked by lozenge in Figure) are attributed to the 111, 200, 220, 311 and 222 reflections of the metal nanoparticles [38,39].

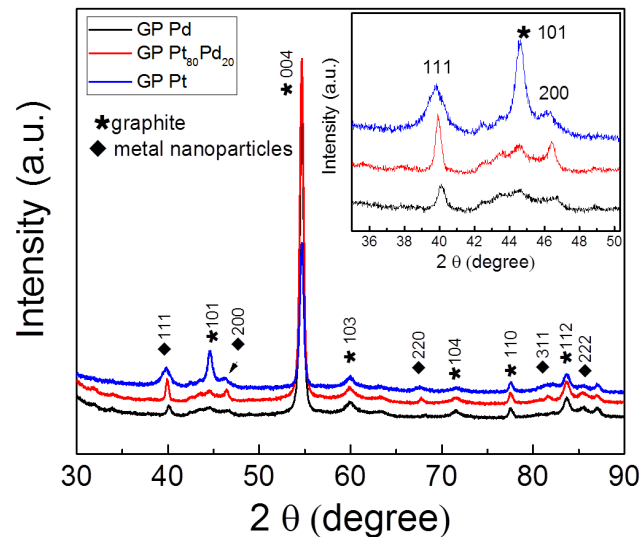


Figure 4. XRD patterns of platinum, palladium, Pt₈₀Pd₂₀ nanoparticles supported onto graphene paper.

The inset shows the enlarged region containing the most intense 111 and 200 peaks of metal nanoparticles. The 111 and 200 reflection peaks were found at 39.82°, 46.08° for the platinum, and at 40.13°, 46.62° for palladium, and match those of Face-Centered Cubic (FCC) structure of platinum (JCPDF 04-0802) and of palladium (JCPDF 46-1043), respectively. The Pt₈₀Pd₂₀ NPs show the 111 and 200 reflection peaks at 39.94° and 46.43°, respectively. According to the composition of the intermetallic nanoparticles, the latter values are included between those of the two pure metals. The XRD results show the crystalline nature of all of the NPs considered here. In particular, the width and position of the peak 111 reflect the different composition and average size of the metallic NPs [38]. Furthermore, the present bimetallic NPs structure does not show the core-shell type, as described elsewhere [30].

3.3. Surface and Electronic Structure of NPs

The surface of the Pd-GP, Pt-GP and Pt₈₀Pd₂₀-GP have been investigated by XPS, which provides information on the electronic structure and allows estimation of the surface elemental composition, once the relevant atomic sensitivity factors have been taken into account [32,33,40,41].

Figure 5a shows the XPS of the Pd-GP in the Pd 3d binding energy region. The spectrum was deconvoluted with the superposition of two doublet components; a dominating doublet at 335.5 and 340.8 eV (5.3 eV spin-orbit coupling) is associated to the 3d_{5/2,3/2} of metallic palladium (Pd⁰) states and a doublet at 337.5 and 342.8 eV (5.3 eV spin-orbit coupling) is associated to Pd(II) due to a partial surface oxidation of palladium [42,43].

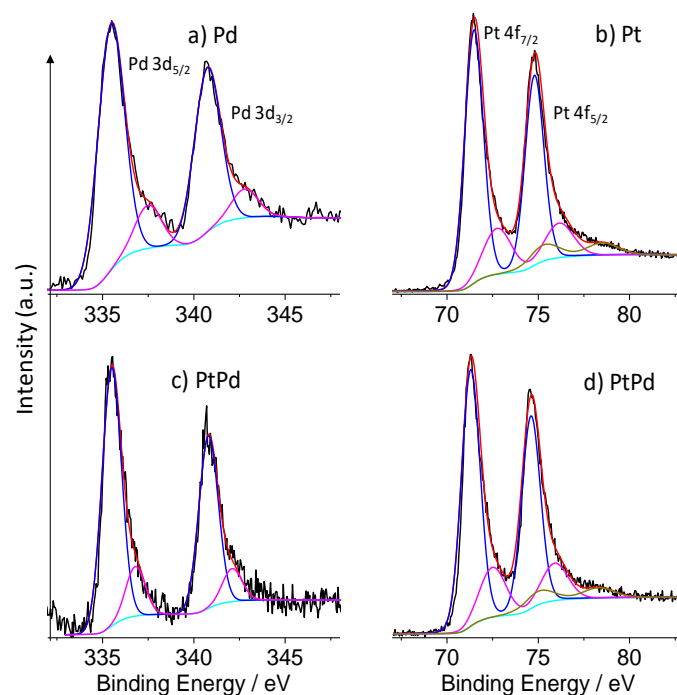


Figure 5. Al-K α excited photoelectron spectra of Pd 3d binding energy region of: (a) Pd-GP and (c) Pt₈₀Pd₂₀-GP. The 3d_{5/2}—3d_{3/2} spin-orbit doublets (blue and magenta line) refer to the Pd⁰ and Pd(II) states, respectively; 4f binding energy region of: (b) Pt-GP and (d) Pt₈₀Pd₂₀-GP. The 4f_{7/2}—4f_{5/2} spin-orbit doublets (blue, magenta and dark yellow line) refer to Pt⁰, Pt(II) and Pt(IV) states, respectively. The cyan line refers to the background and the red line superimposed to the experimental black profile refers to the sum of all of the Gaussian components.

Figure 5b shows the XPS of the Pt-GP in the Pt 4f binding energy region. The XPS spectra of Pt 4f were deconvoluted using three doublet components. The main doublet at 71.3 and 74.6 eV (3.3 eV spin-orbit coupling) is assigned to the 4f_{7/2,5/2} of zero valent Pt⁰ [44], while the doublet at 72.6 and 76.0 eV (3.4 eV spin-orbit coupling) is attributed to Pt(II) species [44,45]. The higher doublet at 75.2 and 78.5 eV (3.3 eV spin-orbit coupling) is assigned to Pt(IV) species [45].

Figure 5c shows the XPS of the Pt₈₀Pd₂₀-GP in the Pd 3d binding energy region. The Pd 3d level was deconvoluted with the superposition of two doublet components: a dominating doublet at 335.5 and 340.8 eV (5.3 eV spin-orbit coupling) is associated to the metallic palladium (Pd⁰) states, and the doublet at 336.8 and 342.1 eV (5.3 eV spin-orbit coupling) is associated to Pd(II) due to a partial surface oxidation of palladium [42,43]. Gaussian relative intensities are almost coincident with those observed for the Pd-graphene sample, but the higher binding energy doublet (336.8–342.1 eV) is at 0.7 lower binding energy values with respect to that observed for the Pd-graphene-sample. This observation agrees with the somewhat larger electronegativity of palladium (1.40) with respect to that of platinum (1.35) and highlights the establishment of a chemical bond between the two metals that results in electron donation from platinum to palladium.

Figure 5d shows the XPS of the Pt₈₀Pd₂₀-GP sample in the Pt 4f binding energy region. The XPS spectrum of Pt 4f was deconvoluted using three doublet components. The main doublet at 71.3 and 74.6 eV (3.3 eV spin-orbit coupling) is assigned to the zero valent Pt⁰ [44], while the doublet at 72.5 and 75.9 eV (3.4 eV spin-orbit coupling) is attributed to Pt(II) species [44,45]. The higher doublet at 75.0 and 78.3 eV (3.3 eV spin-orbit coupling) is assigned to Pt(IV) species [45]. Both B.E. values and Gaussian relative intensities are similar to those observed for the Pt-GP sample. Table 1 summarizes the component position used in the spectra deconvolution.

Table 1. Position (Binding Energy/eV) of the peak components used in the deconvolution of the spectra reported in Figures 5 and 6.

Sample	C 1s			O 1s			Pt 4f _{7/2,5/2}			Pd 3d _{5/2,3/2}	
	C <i>sp</i> ²	C-OH	C=O	O-C=O	C-O _x H	H ₂ O	Pt ⁰	Pt(II)	Pt (IV)	Pd ⁰	Pd(II)
Pd-GP	284.6	285.8	287.1	288.4	531.5	535.5	-	-	-	335.5/340.8	337.5/342.8
Pt-GP	284.6	286.0	287.1	288.3	531.1	533.1	71.3/74.6	72.6/76.0	75.2/78.5	-	-
Pt ₈₀ Pd ₂₀ GP	284.6	285.7	286.9	288.5	531.8	534.0	71.3/74.6	72.5/75.9	75.0/78.3	335.5/340.8	336.8/342.1

Figure 6a,b show the high-resolution XPS of the Pd-GP in the C 1s and O 1s binding energy (B.E.) regions, respectively. A careful fitting of the experimental profile of the C 1s signal required four Gaussian components centered at 284.6, 285.8, 287.1 and 288.4 eV, respectively (Figure 6a and Table 1). The first component (284.6 eV) is due to *sp*² carbon states [45,46]. The other peaks at 285.8, 287.1 and 288.4 eV are assigned to the C-OH, C=O and O-C=O functional groups present on the surface of the graphene paper [46,47].

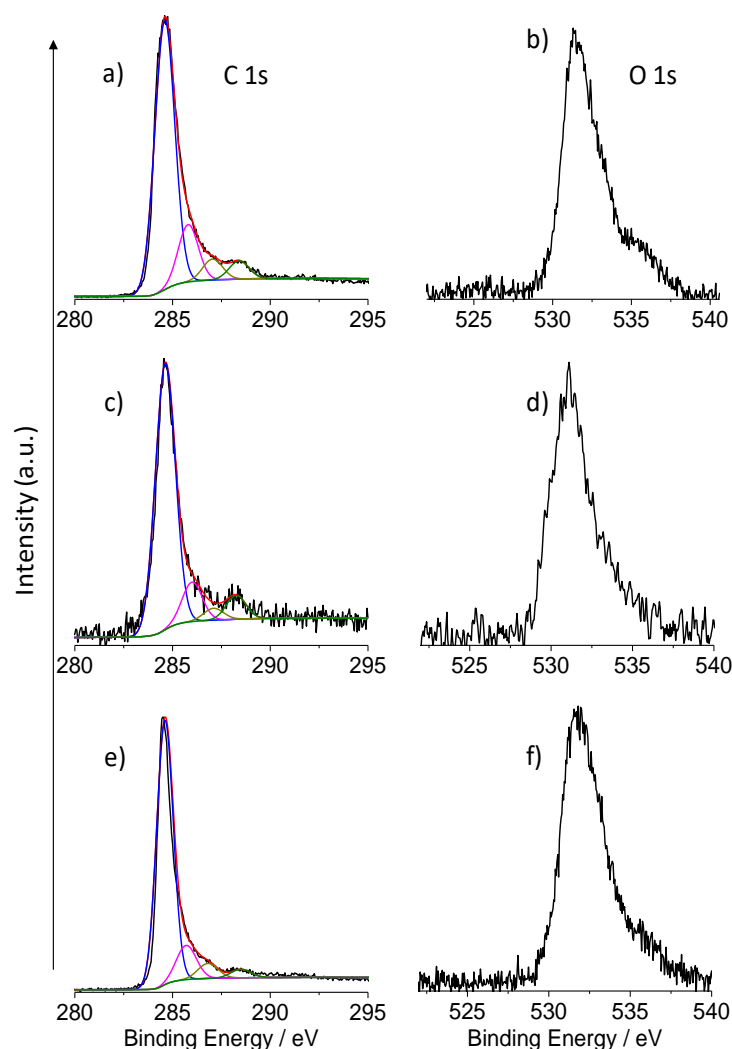


Figure 6. Al-K α excited XPS in the binding energy region of C 1s: (a) Pd-GP; (c) Pt-GP; (e) Pt₈₀Pd₂₀-GP. The component positions are reported in Table 1. O 1s binding energy region of: (b) Pd-GP; (d) Pt-GP; (f) Pt₈₀Pd₂₀-GP.

The XPS peak in the O 1s core level binding energy (Figure 6b) is centered at 531.5 eV and shows some high energy broadening that clearly points to the presence of more components due to O-C=O and -OH groups of the graphene surface, to the oxygen-bonded

to palladium (Pd-O) and to the overlapping Pd 3p_{3/2} spin-orbit component of the Pd metal [48,49]. The additional high binding energy shoulder at 535.5 eV is attributed to the presence of some H₂O molecules on the sample surface [32].

Figure 6c shows the high-resolution XPS of the Pt-GP in the C 1s energy region. An accurate fitting of the spectrum revealed the presence of four components at 284.6, 286.0, 287.1 and 288.3 eV, respectively. These components are at B.E. values similar to those observed for the Pd-graphene sample and due to the same electronic states. The main difference with respect to the previous related XPS results is due to a decreased relative intensity of the component at 287.1 eV (due to the C=O graphene substituent).

The main O 1s signal for the Pd-GP (Figure 6d) lies at 531.1 and is due to the O-C=O groups of the graphene surface and to the oxygen-bonded Pt (Pt-O). The additional high binding energy shoulder is attributed to -OH groups and some water molecules on the graphene surface [48].

Figure 6e shows the high-resolution XPS of the Pt₈₀Pd₂₀-GP in the C 1s energy region. An accurate fitting of the spectrum profile revealed the presence of four components at 284.6, 285.7, 286.9 and 288.5 eV, respectively. These components are at B.E. values similar to those observed for the Pd-graphene and Pt-graphene samples and due to the same electronic states. The main difference with respect to the previous related XPS results is due to a decreased relative intensity of the last component (288.5 eV, due to the O-C=O graphene substituent). This datum is likewise in agreement with the lower oxygen atomic concentration (Table 2).

Table 2. Composition of the surfaces of the NPs-GP systems obtained by XPS (atomic concentration %).

Sample	C 1s (tot.)	O 1s (tot.)	Pt 4f _{7/2,5/2} Pt ⁰ +Pt(II)+Pt(IV)	Pd 3d _{3/2,1/2} Pd ⁰ +Pd(II)
Pd	75.5	22.9	-	1.6
Pt	49.2	20.9	29.9	-
Pt ₈₀ Pd ₂₀	80.3	16.4	2.0	1.3

Figure 6f shows the O 1s spectrum for the Pt₈₀Pd₂₀-GP sample. The O 1s core level centred at 531.8 eV shows some broadening that clearly points to the presence of more components due to O-C=O and -OH groups of the graphene surface, to the oxygen-bonded to platinum (Pt-O) and to palladium (Pd-O) and to the overlapping Pd 3p_{3/2} spin-orbit component of the Pd metal. The additional high binding energy shoulder at 534.0 eV is attributed to the presence of some H₂O molecules on the sample surface [32]. Table 2 reports the surface composition obtained by the XPS analyses. Notable, the platinum content in the Pt-GP is higher than that of palladium and platinum in the respective Pd-GP and Pt₈₀Pd₂₀-GP systems. The data reflect the nominal amount of NPs casted onto the surface of GP (vide experimental section). Moreover, the surface composition of the bimetallic NPs that has the bulk composition of Pt_{68.3}Pd_{31.7} by atomic%, is slightly enriched in palladium with respect to the bulk composition, indicating the presence of the segregation of the latter metal.

3.4. Electro-Sorption and Galvanostatic Charge-Discharge Properties

The hydrogen electro-sorption reaction by the NPs-GP electrodes was performed in alkaline electrolyte. In alkaline electrolyte the reaction is less efficient than that in acidic electrolyte, as consequence of the slow step of reaction consisting in the water dissociation into OH⁻ and H⁺ (Equation (1)) [50]. However, from an industrial point of view, alkaline electrolytes are more interesting since they overcame the problem of expensive proton exchange membranes required in acidic electrolyte [50]. Figure 7a shows the cyclic voltammograms recorded in the potential region comprises between -1 and 0.4 V by the NPs-GP nanoelectrode arrays based on platinum, palladium or Pt₈₀Pd₂₀. For comparison, the voltammogram obtained by the GP alone was included in the Figure. In alkaline electrolyte hydrogen ions are adsorbed and reduced onto the metal surface

according to the Volmer-Heyrovsky mechanism summarized by Equations (1) and (2), where M represents the metals or Pt₈₀Pd₂₀ alloy [51].

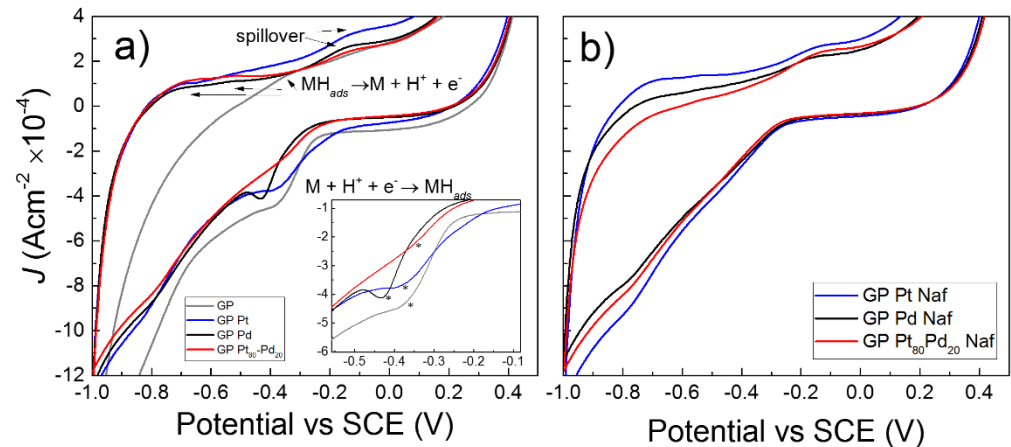


Figure 7. (a) Cyclic voltammograms of GP and NPs-GP; (b) cyclic voltammograms of NPs-GP obtained by suspension in water 0.25% wt. Nafion. Conditions: KOH 1 M; scan rate 20 mVs⁻¹. The inset shows the peak position of hydrogen ion adsorption and reduction, marked by asterisk.

The peaks associated with the adsorption and reduction of the H⁺ ions were found at potentials vs. SCE of −0.38 V (GP alone), −0.37 V (Pt), −0.43 V (Pd), and −0.35 V (Pt₈₀Pd₂₀), respectively. The inset in Figure reports enlarged portion of voltammograms containing the peak position marked by asterisk. The peak of H⁺ adsorption and reduction by the bimetallic alloy has the lowest potential value, showing a greater efficiency of this system with respect to the others in the catalysis of this process. According to the Butler-Volmer Equation, the shift of the cathodic peak towards higher potential values is accompanied by an increase of its full width at half maximum (FWHM). Thus, the peak of hydrogen reduction in the voltammogram by bimetallic system is characterized by larger width, compared to the peaks obtained by the platinum or palladium single catalysts [52]. The peaks of hydrogen desorption and oxidation to H⁺ ion are located at potentials of −0.31 V (GP alone), −0.68 and −0.49 V (Pt), −0.68 and −0.53 V (Pd), −0.64, and 0.53 V (Pt₈₀Pd₂₀), respectively. Conversely to what observed in the voltammogram of GP alone, the voltammograms of the NPs-GP electrodes show two anodic peaks that are attributable to the mechanism involving the desorption of MH_{ads} and oxidation of the H· radical to the H⁺ ion on different crystallographic planes of the NPs surface [53]. Notably, additional peak at about −0.13 V for all systems containing NPs is visible in the voltammograms. This peak is attributable to a significant process of hydrogen spillover present in the investigate systems [54]. With the spillover mechanism, the hydrogen passes from the NPs to the GP, which represents the main absorber for storage (Equation (3)).



Notable, due to the nature of hybrid nanoelectrode array of these systems, the peaks present in the voltammograms are not well pronounced [55]. This is further evident in voltammograms of the systems obtained using Nafion (Figure 7b), that are characterized by finely dispersion of the metal NPs.

Further investigation of the electrochemical properties of the systems was carried out by galvanostatic charge and discharge measurements. Figure 8a shows the galvanostatic charge and discharge curves obtained by the various NPs-GP systems, in comparison to

the GP alone. The Figure reports the electrode potential as function of the specific capacity. In this experiment, the electrodes were charged at a capacity up to 7.8 Ahg^{-1} and then discharged. We reported the fifth cycle of charge–discharge processes when the stabilization of the electrode potential occurs. The specific capacity was calculated on the basis of Faraday’s law, taking into account the mass of 1 cm^2 of graphene paper [56–58]. At this value of specific capacity, the condition of potential stabilization is reached both in the charge as well as in the discharge curves. From the curves of Figure 8a it can be seen that at the initial stage of both charge and discharge processes (e.g., roughly for the first 4 Ahg^{-1}), the Pt-GP system assumes potentials greater than that of the GP alone, showing higher kinetics (as expected for the presence of the catalysis offered by the platinum nanoparticles). The Pd-GP systems and, in particular, Pt₈Pd₂₀-GP are further efficient with respect to the charging and discharging processes even with respect to the Pt-GP. This is particularly evident if we take into account the different amount of NPs casted per square centimeter of GP (vide experimental section). In particular, assuming that the charge is entirely used for the reduction reaction of H^+ , in agreement to that assumed in previous works, [56–58] it is possible to obtain that the percentage of hydrogen developed at the steady state potential of polarization curves, accumulated or transferred to the GP, is equal to 1 wt.% for the platinum, and 6 wt.% both for the palladium and the bimetallic Pt₈₀Pd₂₀ (vide later on Table 3). It is worthy of notice that, since the GP used in this study has a thickness of $240 \mu\text{m}$, it is likely that it mainly acts as a conductor of the electrical charges, while only a very thin layer close to the electrical double layer is involved in the hydrogen absorption process [59].

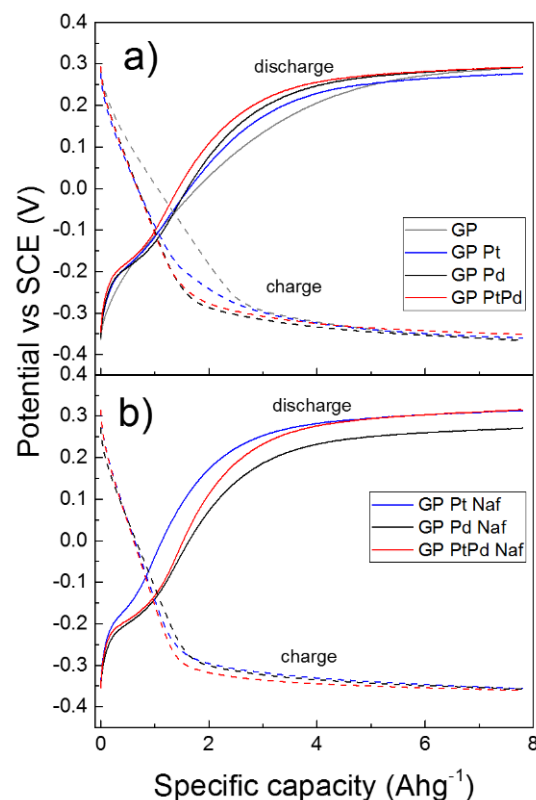
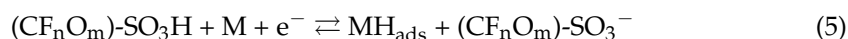
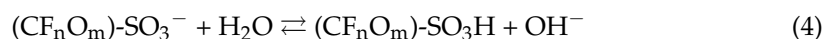


Figure 8. (a) galvanostatic charge and discharge curves of GP and NPs-GP; (b) galvanostatic charge and discharge of NPs-GP obtained by suspension in water 0.25% wt. Nafion. Conditions: KOH 1 M; current $100 \mu\text{A}$. The specific capacity was calculated with respect to the mass of 1 cm^2 of GP.

Table 3. Charge—discharge specific capacity (Ahg^{-1}) and Faradaic efficiency of the NPs-GP systems. Conditions: KOH 1 M; current $\pm 100 \mu\text{A}$.

System	Suspension Medium of NPs	Charge (−0.3 V)	Discharge (+0.25 V)	Faradaic Efficiency %
GP alone	-	4.65	2.77	59.6
Pt-GP	water	4.64	2.98	64.2
Pd-GP	water	5.60	3.70	66.1
Pt ₈₀ Pd ₂₀ -GP	water	5.16	4.02	77.9
Pt-GP	water-0.25 wt.% nafion	5.60	4.85	86.6
Pd-GP	water-0.25 wt.% nafion	5.77	2.76	47.8
Pt ₈₀ Pd ₂₀ -GP	water-0.25 wt.% nafion	6.21	4.50	72.4

Figure 8b shows the galvanostatic charge and discharge curves obtained by the NPs-GP systems casted by water-0.25 wt.% Nafion suspension. In these systems the thin layer of Nafion surrounding the NPs surface acts as proton exchange membranes (Equation (4)). In particular, Nafion is H^+ conductive and then increases the activity of hydrogen ions neighbor of the NPs surface (Equation (5)):



where $(\text{CF}_n\text{O}_m)\text{-SO}_3^-$ represents the ionomer in the anionic form and $(\text{CF}_n\text{O}_m)\text{-SO}_3\text{H}$ represents the ionomer interacted with the H^+ . Table 3 reports the electrochemical performances of our systems derived from the curves of Figure 8a,b. In detail, the galvanostatic charge and discharge capacities of the various NPs-GP systems are compared. For the charging capacity calculation, we assumed the start of the charging process when the electrode potential reaches a value of -0.3 V vs. SCE. This value corresponds roughly to the 97% of the steady state potential. In the discharge process the cut-off potential was assumed at 0.25 V vs. SCE that corresponds to 90% of the steady state potential. Faradaic efficiency was calculated by the percentage of the ratio discharge to charge capacities, according to previous reported study [58]. Clearly, palladium and Pt₈₀Pd₂₀ show the highest values of charge and discharge capacities, with a Faradaic efficiency of about 78 % for the bimetallic system. In presence of Nafion the highest charge capacity is still shown by the bimetallic system with a Faradaic efficiency of about 72%. The highest efficiency is presented by the platinum system with a value of 86.6%. This finding is related to the platinum NPs dispersion operated by the Nafion, according to the morphology reported in Figure 2d. However, XPS analyses revealed that the platinum surface concentration in Pt-GP is 18 times higher than that of palladium in Pd-GP and 9 times higher than that of the sum of palladium and platinum in the bimetallic system (vide Table 2). Then, the highest charge-discharge capacity is presented by the systems containing palladium. Moreover, the high ability to reduce the H^+ ion and thus the charge capacity of the bimetallic system, according to the XPS data, is consistent with the interaction between the two metals that results in an electron donation from platinum to palladium. Table 4 reports the performances of hydrogen evolution and adsorption of the nanoelectrode arrays, described in this work, in comparison with some platinum and palladium nanoparticles-decorated carbon nanomaterials reported in literature. Since the literature data concerning the hydrogen electro-sorption and storage are often inhomogeneous, we have reported only those parameters that can be compared. In particular, Table 4 compares some nanosystems obtained by conventional chemical reduction with those obtained by PLAL. Furthermore, the fifth column of the Table 4 shows the absorption data at the pressure of 1 bar and ambient temperature, obtained by gaseous phase chemical reaction or by electro-sorption reaction, respectively. The comparison of the data shows that our systems are competitive with respect to the other state of the art materials, also taking into account the ease of preparation method proposed and the low environmental impact presented by the synthesis process, which does not involve the

formation of harmful chemical synthesis waste. Furthermore, our data, according to the literature, confirm the superior performances of palladium-based nanosystems compared to platinum-based ones towards the electro-sorption reaction of H^+ .

Table 4. Performances of hydrogen evolution and adsorption of the systems described in this work in comparison with some platinum and palladium nanoparticles-decorated carbon nanomaterials reported in literature.

System	Electrode	Metal NPs Production Method	Electrolyte (ElectroChemical Method) or Gaseous Phase Reaction of H_2 Adsorption	Hydrogen Storage/Evolution (Wt.%)	Faradaic Efficiency (%)	Reference
Pd NPs/nafion	GCE	Wet/ $NaBH_4$	H_2SO_4	0.003	83.1	[52]
Pd-rGO/nafion	GCE	Wet/ $NaBH_4$	H_2SO_4	0.14	85	[52]
Pd/B-rGO/nafion	GCE	Wet/ $NaBH_4$	H_2SO_4	0.35	95	[52]
Pt- (GO)/HKUST-1	-	Wet/Ethylene glycol	Gaseous phase reaction	1.6	-	[12]
Pt Covalent triazine framework(CTF-N)	Fluorine doped tin oxide (FTO)	Wet/ $NaBH_4$	Trietanolamine ⁽¹⁾	0.2	-	[16]
Pd Covalent triazine framework(CTF-N)	Fluorine doped tin oxide (FTO)	Wet/ $NaBH_4$	Trietanolamine ⁽¹⁾	1.05	-	[16]
Ni/rGO	-	Reduction in H_2 ⁽²⁾	Gaseous phase reaction	0.007	-	[60]
Ni/Pd/rGO,	-	Reduction in H_2 ⁽²⁾	Gaseous phase reaction	0.13	-	[60]
Ni/Ag/Pd/rGO	-	Reduction in H_2 ⁽²⁾	Gaseous phase reaction	0.055	-	[60]
Pd/graphene	-	Reduction in H_2 ⁽²⁾	Gaseous phase reaction	8.67 ⁽³⁾	-	[4]
Pd/MWCNT	-	PLAL	Gaseous phase reaction	1.2	-	[61]
Pt-GP	GP	PLAL	KOH	1	64.2	This work
Pd-GP	GP	PLAL	KOH	6	66.1	This work
Pt ₈₀ Pd ₂₀ -GP	GP	PLAL	KOH	6	77.9	This work
Pt-GP/nafion	GP	PLAL	KOH	1	86.6	This work
Pd-GP/nafion	GP	PLAL	KOH	6	47.8	This work
Pt ₈₀ Pd ₂₀ -GP/nafion	GP	PLAL	KOH	6	72.4	This work

⁽¹⁾ Photoelectrochemical method; ⁽²⁾ reduction at 300 °C, H_2 atmosphere; ⁽³⁾ value referred to a pressure of 60 bar, otherwise unspecified values were measured at 1 bar.

4. Conclusions

In this work we propose new nanoelectrode arrays for the electro-sorption of hydrogen in an alkaline electrolyte. The nanoelectrodes consist of hybrid metal NPs-decorated graphene paper. A comparative study between naked and surrounded by a thin layer of perfluoro-sulfone ionomer metal NPs has been described. Graphene paper is a lightweight carbon-based material having a high defect density that facilitates the allocation of hydrogen both as H_2 or H by spillover mechanism. Metal NPs increase the Faradaic efficiency of the GP electrodes. The studied systems are suitable both for the production via water splitting as well as for the storage of hydrogen. The metal NPs act as catalysts for the evolution of hydrogen through the reduction of H^+ and the GP acts as a lightweight and efficient hydrogen storage system. Significant spillover mechanism was clearly identified by the cyclic voltammograms. We described in this study that palladium surface segregation observed in the Pt₈₀Pd₂₀ and the electron donation from platinum to palladium increases the electro-catalytic efficiency of this system both in the charge as well as in the discharge processes with respect to the single metals alone. The Faradaic efficiency is also increased. The most significant effects of the ionomer consist mainly in the promotion of the NPs dispersion onto the surface of GP and in the increase of the ionic activity of H^+ close to the NPs surface. Taking into account the different amount of platinum, palladium and Pt₈₀Pd₂₀ NPs in the studied electrodes, the latter two systems show the highest charge-discharge capacities. Furthermore, the ionomer acts as H^+ selective membrane producing an evident increase of the charge-discharge capacities of the hybrid electrodes in alkaline electrolyte. In future work a thinner GP support will be taken into account to increase the energy density of the proposed nanoelectrode arrays.

Author Contributions: Conceptualization, F.R. and A.S.; methodology, A.S., M.C. and F.R.; formal analysis, A.S., F.R., M.C. and A.G.; investigation, A.S., F.R., M.C. and A.G.; resources, F.R. and M.G.G.; data curation, A.S., F.R., M.C. and A.G.; writing—original draft preparation, A.S.; writing—review and editing, A.S., F.R. and A.G.; supervision, F.R.; project administration, F.R. and M.G.G.; funding acquisition, F.R. and M.G.G. All authors have read and agreed to the published version of the manuscript.

Funding: This work was supported by the projects: Programma di ricerca di Ateneo UNICT 2020-22 linea 2. A.G. thanks the Pia.ce.ri. project “MAF-moF”.

Institutional Review Board Statement: Not applicable.

Informed Consent Statement: Not applicable.

Data Availability Statement: Not applicable.

Acknowledgments: The authors wish to thank the Bio-nanotech Research and Innovation Tower (BRIT) Laboratory of the University of Catania (Grant no. PONa3_00136 financed by the MIUR) for the Smartlab diffractometer and XPS facilities, and Simona Boninelli (Institute for Microelectronics and Microsystems of National Research Council of Italy CNR-IMM, Zona Industriale—Strada VIII n°5, 95121 Catania, Italy) for the TEM analysis.

Conflicts of Interest: The authors declare no conflict of interest.

References

1. Nassar, N.T.; Brainard, J.; Gulley, A.; Manley, R.; Matos, G.; Lederer, G.; Bird, L.R.; Pineault, D.; Alonso, E.; Gambogi, J.; et al. Evaluating the mineral commodity supply risk of the U.S. manufacturing sector. *Sci. Adv.* **2020**, *6*, eaay8647. [[CrossRef](#)] [[PubMed](#)]
2. Ali, S.; Giurco, D.; Arndt, N.; Nickless, E.; Brown, G.; Demetriades, A.; Durrheim, R.; Enriquez, M.; Kinnaird, J.; Littleboy, A.; et al. Mineral supply for sustainable development requires resource governance. *Nature* **2017**, *543*, 367–372. [[CrossRef](#)] [[PubMed](#)]
3. Boretti, A.; Rosa, L. Reassessing the projections of the World Water Development Report. *NPJ Clean Water* **2019**, *2*, 15. [[CrossRef](#)]
4. Chukwudi Tashie-Lewis, B.; Godfrey Nnabuife, S. Hydrogen Production, Distribution, Storage and Power Conversion in a Hydrogen Economy—A Technology Review. *J. Adv. Chem. Eng.* **2021**, *8*, 100172. [[CrossRef](#)]
5. Boateng, E.; Chen, A. Recent advances in nanomaterial-based solid-state hydrogen storage. *Mater. Today Adv.* **2020**, *6*, 100022. [[CrossRef](#)]
6. Navlani-García, M.; Mori, K.; Kuwahara, Y.; Yamashita, H. Recent strategies targeting efficient hydrogen production from chemical hydrogen storage materials over carbon-supported catalysts. *NPG Asia Mater.* **2018**, *10*, 277–292. [[CrossRef](#)]
7. Andersson, J.; Gronkvist, S. Large-scale storage of hydrogen. *Int. J. Hydrogen Energy* **2019**, *44*, 11901–11919. [[CrossRef](#)]
8. Li, X.; Zhao, L.; Yu, J.; Liu, X.; Zhang, X.; Liu, H.; Zhou, W. Water Splitting: From Electrode to Green Energy System. *Nano-Micro Lett.* **2020**, *12*, 131. [[CrossRef](#)]
9. Mohan, M.; Kumar Sharma, V.; Anil Kumar, E.; Gayathri, V. Hydrogen storage in carbon materials—A review. *Energy Storage* **2019**, *1*, e35. [[CrossRef](#)]
10. Wang, H.; Gao, Q.; Hu, J. High Hydrogen Storage Capacity of Porous Carbons Prepared by Using Activated Carbon. *J. Am. Chem. Soc.* **2009**, *131*, 7016–7022. [[CrossRef](#)]
11. Schilter, D. Hydrogen Storage: A reformed approach. *Nat. Rev. Chem.* **2017**, *1*, 0027. [[CrossRef](#)]
12. Li, J.; Cheng, Y.; Zhang, J.; Fu, J.; Yan, W.; Xu, Q. Confining Pd Nanoparticles and Atomically Dispersed Pd into Defective MoO₃ Nanosheet for Enhancing Electro- and Photocatalytic Hydrogen Evolution Performances. *ACS Appl. Mater. Interfaces* **2019**, *31*, 27798–27804. [[CrossRef](#)] [[PubMed](#)]
13. Zhou, H.; Liu, X.; Zhang, J.; Yan, X.; Liu, Y.; Yuan, A. Enhanced room-temperature hydrogen storage capacity in Pt-loaded graphene oxide/HKUST-1 composites. *Int. J. Hydrogen Energy* **2014**, *39*, 2160–2167. [[CrossRef](#)]
14. Faye, O.; Szpunar, J.; Szpunar, B.; Beye, A. Hydrogen adsorption and storage on Palladium—Functionalized graphene with NH-dopant: A first principles calculation. *Appl. Surf. Sci.* **2017**, *392*, 362–374. [[CrossRef](#)]
15. Qu, D.; Zhu, X.; Zheng, D.; Zheng, Y.; Liu, D.; Xie, Z.; Tang, H.; Wen, J.; You, X.; Xiao, L.; et al. Improve Electrochemical Hydrogen Insertion on the Carbon Materials Loaded with Pt nano-particles through H spillover. *Electrochim. Acta* **2015**, *174*, 400–405. [[CrossRef](#)]
16. Oh, J.; Bathula, H.B.; Park, J.H.; Suh, Y. A sustainable mesoporous palladium-alumina catalyst for efficient hydrogen release from N-heterocyclic liquid organic hydrogen carriers. *Commun. Chem.* **2019**, *2*, 68. [[CrossRef](#)]
17. Liu, M.; Wang, X.; Liu, J.; Wang, K.; Jin, S.; Tan, B. Palladium as a Superior Cocatalyst to Platinum for Hydrogen Evolution Using Covalent Triazine Frameworks as a Support. *ACS Appl. Mater. Interfaces* **2020**, *12*, 12774–12782. [[CrossRef](#)]
18. Hurley, N.; McGuire, S.C.; Wong, S. Assessing the Catalytic Behavior of Platinum Group Metal-Based Ultrathin Nanowires Using X-ray Absorption Spectroscopy. *ACS Appl. Mater. Interfaces* **2021**, *13*, 58253–58260. [[CrossRef](#)]
19. Kobayashi, H.; Yamauchi, M.; Kitagawa, H.; Kubota, Y.; Kato, K.; Takata, M. On the Nature of Strong Hydrogen Atom Trapping Inside Pd Nanoparticles. *J. Am. Chem. Soc.* **2008**, *130*, 1828–1829. [[CrossRef](#)]

20. Baig, N.; Kammakakam, I.; Falath, W. Nanomaterials: A review of synthesis methods, properties, recent progress, and challenges. *Mater. Adv.* **2021**, *2*, 1821–1871. [[CrossRef](#)]
21. Tsuji, T. Preparation of NPs using laser ablation in liquids: Fundamental aspects and efficient utilization. In *Laser Ablation in Liquid: Principles and Applications in the Preparation of Nanomaterials*; Yang, G., Ed.; Jenny Stanford Publishing: Singapore, 2012; pp. 2027–2257; ISBN 9789814310956.
22. Marzun, G.; Streich, C.; Jendrzey, S.; Barcikowski, S.; Wagener, P. Adsorption of colloidal platinum nanoparticles to supports: Charge transfer and effects of electrostatic and steric interactions. *Langmuir* **2014**, *30*, 11928–11936. [[CrossRef](#)] [[PubMed](#)]
23. Zhang, J.; Oko, D.N.; Garbarino, S.; Imbeault, R.; Chaker, M.; Tavares, A.C.; Guay, D.; Ma, D. Preparation of PtAu alloy colloids by laser ablation in solution and their characterization. *J. Phys. Chem. C* **2012**, *116*, 13413–13420. [[CrossRef](#)]
24. Reichenberger, S.; Marzun, G.; Muhler, M.; Barcikowski, S. Perspective of Surfactant-Free Colloidal Nanoparticles in Heterogeneous Catalysis. *ChemCatChem* **2019**, *11*, 4489–4518. [[CrossRef](#)]
25. Zhang, D.; Gökce, B.; Barcikowski, S. Laser Synthesis and Processing of Colloids: Fundamentals and Applications. *Chem. Rev.* **2017**, *117*, 3990–4103. [[CrossRef](#)] [[PubMed](#)]
26. Liang, S.; Zhang, L.; Reichenberger, S.; Barcikowski, S. Design and perspective of amorphous metal nanoparticles from laser synthesis and processing. *Phys. Chem. Chem. Phys.* **2021**, *23*, 11121–11154. [[CrossRef](#)]
27. Semaltianos, N.G. Nanoparticles by laser ablation of bulk target materials in liquids. In *Handbook of Nanoparticles*; Aliofkhaezrai, M., Ed.; Springer: Cham, Switzerland, 2016; pp. 67–92. [[CrossRef](#)]
28. Hodges, A.; Hoang, A.; Tsekouras, G.; Wagner, K.; Lee, C.-Y.; Swiegers, G.F.; Wallace, G. A high-performance capillary-fed electrolysis cell promises more cost-competitive renewable hydrogen. *Nat. Commun.* **2022**, *13*, 1304. [[CrossRef](#)]
29. Forsythe, R.C.; Cox, C.P.; Wilsey, M.K.; Müller, A.M. Pulsed Laser in Liquids Made Nanomaterials for Catalysis. *Chem. Rev.* **2021**, *121*, 7568–7637. [[CrossRef](#)]
30. Censabella, M.; Torrisi, V.; Boninelli, S.; Bongiorno, C.; Grimaldi, M.G.; Ruffino, F. Laser ablation synthesis of mono- and bimetallic Pt and Pd nanoparticles and fabrication of Pt-Pd/Graphene nanocomposites. *Appl. Surf. Sci.* **2019**, *475*, 494–503. [[CrossRef](#)]
31. Ozmaiana, M.; Naghdabadi, R. Modeling and simulation of the water gradient within a Nafion membrane. *Phys. Chem. Chem. Phys.* **2014**, *16*, 3173. [[CrossRef](#)]
32. Briggs, D.; Grant, J.T. *Surface Analysis by Auger and X-ray Photoelectron Spectroscopy*; IM Publications: Chichester, UK; Surface Spectra Ltd.: Manchester, UK, 2003.
33. Gulino, A. Structural and electronic characterization of self-assembled molecular nanoarchitectures by X-ray photoelectron spectroscopy. *Anal. Bioanal. Chem.* **2013**, *405*, 1479–1495. [[CrossRef](#)]
34. Cristaldi, D.A.; Millesi, S.; Crupi, I.; Impellizzeri, G.; Priolo, F.; Jacobs, R.M.J.; Egdell, R.G.; Gulino, A. Structural, Electronic, and Electrical Properties of an Undoped n-Type CdO Thin Film with High Electron Concentration. *J. Phys. Chem. C* **2014**, *118*, 15019–15026. [[CrossRef](#)]
35. Thompson, M. Xrump. Available online: www.genplot.com (accessed on 22 May 2021).
36. Cuyner, S.; Caillard, A.; Lecas, T.; Bigarré, J.; Buvat, P.; Brault, P. Deposition of Pt inside fuel cell electrodes using high power impulse magnetron sputtering. *J. Phys. D Appl. Phys.* **2014**, *47*, 272001. [[CrossRef](#)]
37. Howe, J.; Rawn, C.; Jones, L.; Ow, H. Improved crystallographic data for graphite. *Powder Diffr.* **2003**, *18*, 150–154. [[CrossRef](#)]
38. Rodríguez-Proenza, C.A.; Palomares-Báez, J.P.; Chávez-Rojo, M.A.; García-Ruiz, A.F.; Azanza-Ricardo, C.L.; Santoveña-Uribe, A.; Luna-Bárceñas, G.; Rodríguez-López, J.L.; Esparza, R. Atomic Surface Segregation and Structural Characterization of PdPt Bimetallic Nanoparticles. *Materials* **2018**, *11*, 1882. [[CrossRef](#)]
39. Higareda, A.; Rosas, G.; Pérez, R.; Esparza, R. Characterization and Electrocatalytic Features of PtPd and PdPt Bimetallic Nanoparticles for Methanol Electro-oxidation. *ChemNanoMat* **2021**, *7*, 958. [[CrossRef](#)]
40. Spitaleri, L.; Gangemi, C.; Purrello, R.; Nicotra, G.; Trusso Sfrassetto, G.; Casella, G.; Casarin, M.; Gulino, A. Covalently Conjugated Gold-Porphyrin Nanostructures. *Nanomaterials* **2020**, *10*, 1644. [[CrossRef](#)]
41. Zimbone, M.; Cacciato, G.; Spitaleri, L.; Egdell, R.G.; Grimaldi, M.G. A Gulino, Sb-doped titanium oxide: A rationale for its photocatalytic activity for environmental remediation. *ACS Omega* **2018**, *3*, 11270–11277. [[CrossRef](#)]
42. Guo, K.; Rowland, L.J.; Isherwood, L.H.; Glodan, G.; Baidak, A. Photon-induced synthesis of ultrafine metal nanoparticles on graphene as electrocatalysts: Impact of functionalization and doping. *J. Mater. Chem. A* **2020**, *8*, 714. [[CrossRef](#)]
43. Fiorenza, R.; Spitaleri, L.; Gulino, A.; Scirè, S. Ru–Pd Bimetallic Catalysts Supported on CeO₂-MnO_x Oxides as Efficient Systems for H₂ Purification through CO Preferential Oxidation. *Catalysts* **2018**, *8*, 203. [[CrossRef](#)]
44. Zheng, J.-N.; Lv, J.-J.; Li, S.-S.; Xue, M.-W.; Wang, A.-J.; Feng, J.-J. One-pot synthesis of reduced graphene oxide supported hollow Ag@Pt core-shell nanospheres with enhanced electrocatalytic activity for ethylene glycol oxidation. *J. Mater. Chem. A* **2014**, *2*, 3445. [[CrossRef](#)]
45. Yen, M.-Y.; Teng, C.-C.; Hsiao, M.-C.; Liu, P.-I.; Chuang, W.-P.; Ma, C.M.; Hsieh, C.-K.; Tsai, M.-C.; Tsai, C.-H. Platinum nanoparticles/graphene composite catalyst as a novel composite counter electrode for high performance dye-sensitized solar cells. *J. Mater. Chem.* **2011**, *21*, 12880–12888. [[CrossRef](#)]
46. Gao, G.; Liu, D.; Tang, S.; Huang, C.; He, M.; Guo, Y.; Sun, X.; Gao, B. Heat-Initiated Chemical Functionalization of Graphene. *Sci. Rep.* **2016**, *6*, 20034. [[CrossRef](#)] [[PubMed](#)]
47. Johra, F.T.; Lee, J.-W.; Jung, W.-G. Facile and safe graphene preparation on solution based platform. *J. Ind. Eng. Chem.* **2014**, *20*, 2883–2887. [[CrossRef](#)]

48. Giofrè, S.V.; Tiecco, M.; Celesti, C.; Patanè, S.; Triolo, C.; Gulino, A.; Spitaleri, L.; Scalse, S.; Scuderi, M.; Iannazzo, D. Eco-Friendly 1,3-Dipolar Cycloaddition Reactions on Graphene Quantum Dots in Natural Deep Eutectic Solvent. *Nanomaterials* **2020**, *10*, 2549. [[CrossRef](#)]
49. Militello, M.C.; Simko, S.J. Elemental Palladium by XPS. *Surf. Sci. Spectra* **1994**, *3*, 387. [[CrossRef](#)]
50. Yuan, L.; Liu, S.; Xu, S.; Yang, X.; Bian, J.; Lv, C.; Yu, Z.; He, T.; Huang, Z.; Boukhvalov, D.W.; et al. Modulation of Volmer step for efficient alkaline water splitting implemented by titanium oxide promoting surface reconstruction of cobalt carbonate hydroxide. *Nano Energy* **2021**, *82*, 105732. [[CrossRef](#)]
51. Kronberg, R.; Lappalainen, H.; Laasonen, K. Revisiting the Volmer–Heyrovsky´ mechanism of hydrogen evolution on a nitrogen doped carbon nanotube: Constrained molecular dynamics versus the nudged elastic band method. *Phys. Chem. Chem. Phys.* **2020**, *22*, 10536. [[CrossRef](#)]
52. Dickinson, E.; Wain, A.J. The Butler-Volmer equation in electrochemical theory: Origins, value, and practical application. *J. Electroanal. Chem.* **2020**, *872*, 114145. [[CrossRef](#)]
53. Farfour, N.; Chbihi, M.; Takky, D.; Eddahaoui, K.; Benmokhtar, S. Catalytic oxidation of methanol on Pt/X (X = CaTP, NaTP) electrodes in sulfuric acid solution. *Mediterr. J. Chem.* **2013**, *2*, 595–606. [[CrossRef](#)]
54. Zhan, D.; Velmurugan, J.; Mirkin, M.V. Adsorption/Desorption of Hydrogen on Pt Nanoelectrodes: Evidence of Surface Diffusion and Spillover. *J. Am. Chem. Soc.* **2009**, *131*, 14756–14760. [[CrossRef](#)]
55. Welch, C.M.; Compton, R.G. The use of nanoparticles in electroanalysis: A review. *Anal. Bioanal. Chem.* **2006**, *384*, 601–619. [[CrossRef](#)] [[PubMed](#)]
56. Oberoi, A.S.; Nijhawan, P.; Singh, P. A Novel Electrochemical Hydrogen Storage-Based Proton Battery for Renewable Energy Storage. *Energies* **2019**, *12*, 82. [[CrossRef](#)]
57. Mosavati, N.; Young, K.-H.; Meng, T.; Simon Ng, K.Y. Electrochemical Open-Circuit Voltage and Pressure-Concentration-Temperature Isotherm Comparison for Metal Hydride Alloys. *Batteries* **2016**, *2*, 6. [[CrossRef](#)]
58. Boateng, E.; Dondapati, J.S.; Thirupathi, A.R.; Chen, A. Significant enhancement of the electrochemical hydrogen uptake of reduced graphene oxide via boron-doping and decoration with Pd nanoparticles. *Int. J. Hydrogen Energy* **2020**, *45*, 28951–28963. [[CrossRef](#)]
59. Dubouis, N.; Grimaud, A. The hydrogen evolution reaction: From material to interfacial descriptors. *Chem. Sci.* **2019**, *10*, 9165–9181. [[CrossRef](#)]
60. Wei, L.; Mao, Y. Enhanced hydrogen storage performance of reduced graphene oxide hybrids with nickel or its metallic mixtures based on spillover mechanism. *Int. J. Hydrogen Energy* **2016**, *41*, 11692–11699. [[CrossRef](#)]
61. Mehrabi, M.; Parvin, P.; Reyhani, A.; Mortazavi, S.Z. Hydrogen storage in multi-walled carbon nanotubes decorated with palladium nanoparticles using laser ablation/chemical reduction methods. *Mater. Res. Express* **2017**, *4*, 095030. [[CrossRef](#)]